International Journal of Science and Engineering Applications
Volume 15-Issue 08, 01 – 08, 2026, ISSN:- 2319 - 7560
DOI: 10.7753/IJSEA1508.1001

Quality-Guided and Adaptive DC-Constrained Microseismic Moment Tensor Inversion and Stability Analysis

Ke Pan, Peng Wang*, Bingbing Zhu
Key Laboratory of Exploration Technologies for Oil and Gas Resources, Ministry of Education, Yangtze University, Wuhan, 430100, Hubei, China

Abstract: Under downhole microseismic monitoring conditions, uneven data quality or large velocity-model errors may cause the inversion to misinterpret noise and local waveform-fitting residuals as spurious non-double-couple components such as ISO and CLVD components, thereby affecting the interpretation of microseismic rupture types. To address this problem, on the basis of integrating P-wave and S-wave waveforms, P-wave first-motion polarity, and S/P amplitude ratio information, this paper proposes a more effective microseismic moment tensor inversion method. At the observation level, weights are assigned according to receiver-recording quality and effective signal quality in different frequency bands. At the source-model level, an adaptive DC skeleton constraint is introduced to first identify a relatively stable dominant shear mechanism and then regulate non-double-couple components such as ISO and CLVD. In synthetic-data tests, representative source-type events and a multistage synthetic microseismic event set are separately designed to verify the effectiveness and stability of the proposed method. The results show that the proposed method can effectively suppress the formation of spurious non-double-couple components and can better preserve the DC, ISO, and CLVD component proportions in mixed-type events. Compared with the waveform-matching method and the fixed-weight joint-constrained method, the proposed method maintains physically acceptable solution proportions ranging from 0.77 to 0.86 under noise interference and from 0.66 to 0.86 under velocity perturbation, while also achieving better performance in terms of moment tensor deviation angle and source-type proportion recovery.

Keywords: Downhole microseismic monitoring; moment tensor inversion; quality-guided weighting; adaptive DC skeleton; focal mechanism; non-double-couple component

1. INTRODUCTION

Hydraulic fracturing is a key reservoir-stimulation technology for unconventional oil and gas reservoirs and enhanced geothermal systems [1]. Fluid injection changes pore pressure and the local stress state, inducing rock failure, fracture slip, stress release, and microseismicity [2]. Microseismic monitoring uses event location, magnitude, and focal-mechanism analysis to characterize fracture extension, stimulated reservoir volume, and local stress response [3 – 4]. Event distributions mainly delineate the affected range and fracture-cloud geometry, whereas focal mechanisms provide rupture type, slip direction, volumetric change, and stress information needed to distinguish shear slip, tensile failure, and compound rupture [5]. However, under downhole monitoring conditions, limited aperture, receiver geometry, and variations in phase-recording quality can reduce the stability of focal-mechanism inversion [6].

In downhole observations, receivers deployed in monitoring wells are close to the source and usually acquire three-component records with high signal-to-noise ratios and clear P/S phases, making them suitable for focal-mechanism and moment tensor inversion [5]. Jointly incorporating three-component waveforms, P-wave first-motion polarity, and S/P amplitude ratios strengthens constraints on waveform phase and amplitude, radiation quadrants, and P/S energy partitioning [7–10]. Recent studies have extended downhole inversion toward multi-source-model comparison, distributed acoustic sensing, and reliability assessment of non-DC components [11–13]. Although a full moment tensor model represents source types more completely, its stability remains sensitive to observation geometry and data quality. Limited receiver numbers, insufficient azimuthal coverage, velocity-model errors, coupling differences, and uncertain phase-window picking can degrade waveform, polarity, and amplitude-ratio constraints, leading to non-uniqueness and instability [6].

Therefore, downhole full moment tensor inversion must address two related issues: strengthening mechanism constraints under limited-aperture conditions and preventing low-SNR records, weak effective frequency bands, velocity-model errors, and local residuals from being interpreted as true non-double-couple components. This paper proposes the Quality-Guided Adaptive DC-Constrained Microseismic Moment Tensor Inversion method (QG-ADCC-MTI). At the observation level, receiver-recording quality weights are combined with frequency-band quality modulation to form integrated receiver-band weights, so that three-component waveforms, P-wave first-motion polarity, and S/P amplitude ratios enter the joint objective according to their reliability. During the source-parameter search, a group of high-ranking pure-DC candidates is first extracted to construct the DC core set, which serves as the adaptive skeleton reference. The ISO and CLVD contributions are then regulated according to the explanatory capability of that skeleton. Two groups of synthetic data are used to evaluate source-type recovery and stability. The results show that QG-ADCC-MTI suppresses spurious non-double-couple components in DC-dominated events, preserves reasonable source-type proportions in mixed events, and is more stable than waveform matching and fixed-weight joint inversion under noise and velocity-model perturbations.

2. METHODOLOGY

Full moment tensor inversion estimates the source tensor, from which the DC component can be converted into strike, dip, and rake, while the DC/ISO/CLVD decomposition characterizes the source type. The full moment tensor can be decomposed into DC, ISO, and CLVD components [14–16]. The DC component is converted into nodal-plane parameters and describes shear slip; ISO and CLVD components assist in identifying volumetric change and shear-tensile compound rupture. Compared with pure-DC inversion, the full model can therefore represent shear, tensile, and compound failure, but its additional degrees of freedom require effective control. The framework proposed here extracts waveform, polarity, and amplitude-ratio information from P- and S-wave windows, combines receiver-recording and frequency-band quality into integrated weights, and introduces an adaptive DC skeleton to regulate ISO/CLVD contributions. As shown in Figure 1, the method comprises feature extraction, quality-guided objective construction, adaptive DC-constrained inversion, and solution evaluation.

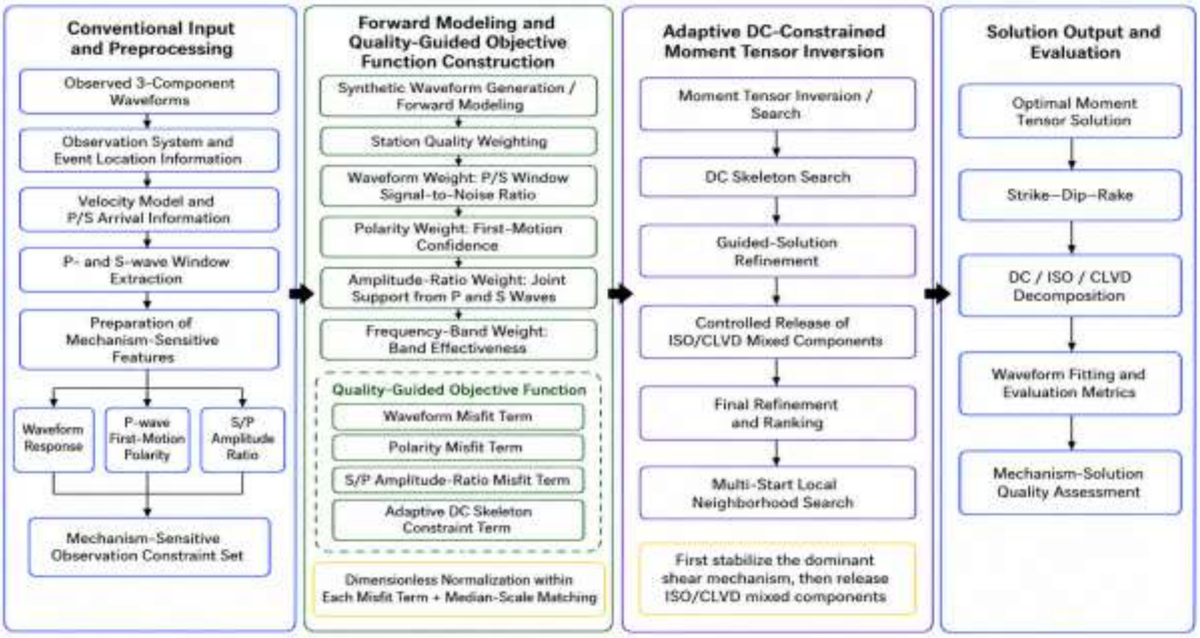

Figure 1. Framework of quality-guided and adaptive DC-constrained microseismic moment tensor inversion.

(1) Feature construction. Three-component records, event and receiver geometry, the velocity model, and P/S arrivals are used to extract P- and S-wave windows in three bands (20–40, 40–60, and 60–80 Hz). Waveforms, P-wave first-motion polarity, and S/P amplitude ratios form the observation constraints.
(2) Quality-guided weighting. Receiver quality and band-dependent signal quality determine the effective weights. Waveform, polarity, amplitude-ratio, and DC-skeleton terms are normalized and balanced by median-scale matching.
(3) Adaptive DC constraint. A search is first performed in the pure-DC subspace to identify a dominant shear mechanism. Its explanatory capability controls the search range and the release of ISO/CLVD components: reliable DC support strengthens the constraint, whereas insufficient support permits controlled non-DC expression.
(4) Output and evaluation. The optimal moment tensor, nodal-plane parameters, source-type proportions, waveform fit, deviation angle, and stability indicators are reported.

2.1 Moment Tensor Source Representation and Mechanism-Sensitive Observation Construction

To transform the above inversion framework into a computable objective function, the response relationship between moment tensor source parameters and observed three-component records is first established [17–19]:

$$u_{i,b,c}^{obs}(t) = \mathrm{B}_b\left[\sum_{k=1}^{6} M_k\left(G_{i,c,k}(t;\gamma) * s(t)\right)\right] + n_{i,b,c}(t), \quad c \in \{Z,R,T\} \tag{1}$$

where i, b, and c denote receiver, frequency band, and component; B_b is the band-pass operator; M_k is the independent component of the moment tensor, $G_{i,c,k}(t;\gamma)$ is the Green's function corresponding to the k-th independent moment tensor component, $s(t)$ is the source time function; and n represents observation and modeling errors. Records are rotated to Z/R/T so that P, SV, and SH radiation is jointly constrained. The full moment tensor is parameterized as:

$$\mathbf{M}(\theta) = M_0\left[\mathbf{M}_{\mathrm{DC}}(s,d,r) + \eta_{\mathrm{iso}}\mathbf{I} + \eta_{\mathrm{clvd}}\mathbf{M}_{\mathrm{CLVD}}\right] \tag{2}$$

where M_0 is the scalar moment; $\mathbf{M}_{\mathrm{DC}}(s,d,r)$ is the normalized DC tensor defined by strike, dip, and rake; $\mathbf{I}$ and $\mathbf{M}_{\mathrm{CLVD}}$ are the ISO and CLVD bases; and η_{iso} and η_{clvd} control their relative contributions. The velocity-scale parameter gamma compensates for small propagation-velocity deviations.
The inversion uses three complementary observations: three-component P/S waveforms, P-wave first-motion polarity, and the logarithmic S/P amplitude ratio. Together they constrain waveform shape, radiation quadrant, and P/S energy partitioning.

2.2 Quality-Guided Weights and Joint Objective Function

Based on the multiple observation constraints, the quality-guided joint objective function is defined as follows:

$$\Phi(\theta) = \lambda_w\Phi_w(\theta) + \lambda_p\Phi_p(\theta) + \lambda_a\Phi_a(\theta) + \lambda_g J_g(\theta) \tag{3}$$

where $\Phi_w(\theta)$, $\Phi_p(\theta)$, and $\Phi_a(\theta)$ are the three-component waveform misfit term, the P-wave first-motion polarity misfit term, and the S/P amplitude-ratio misfit term, respectively; $J_g(\theta)$ is the adaptive DC-skeleton constraint term; and λ_w, λ_p, λ_a, and λ_g are the normalized effective weights.

The three misfit terms are defined as follows:

$$\Phi_w(\theta) = \frac{\sum_{i,b,c} \omega_b q_{i,c}^{w}\left(e_{i,b,c}^{P} + e_{i,b,c}^{S}\right)}{\sum_{i,b,c} \omega_b q_{i,c}^{w} + \delta}, \quad c = \{Z,R,T\} \tag{4}$$

$$\Phi_p(\theta)=\frac{\sum_{i=1}^{N} q_i^p I\left[P_i^{obs}\neq P_i^{syn}(\theta)\right]}{\sum_{i=1}^{N} q_i^p+\delta} \tag{5}$$

$$\Phi_a(\theta)=\frac{\sum_{i=1}^{N} q_i^a \rho\left[\log R_i^{obs}-\log R_i^{syn}(\theta)\right]}{\sum_{i=1}^{N} q_i^a+\delta} \tag{6}$$

where $q_{i,c}^{w}$, q_i^p, and q_i^a are waveform, polarity, and amplitude-ratio quality weights, respectively; ω_b is the effective weight of the b-th frequency band; $e_{i,b,c}^{P}$ and $e_{i,b,c}^{S}$ are the normalized residuals in the P- and S-wave windows, respectively; δ is a small constant used to prevent zero denominators; $I[\cdot]$ is the indicator function; and $\rho(\cdot)$ is a robust penalty function. The use of logarithmic amplitude ratios can reduce the influence of amplitude-scale differences and local extreme values, enabling amplitude-ratio information to participate in the inversion in a more stable form [20].

To account for variations in effective signal quality across frequency bands, the basic frequency-band weights are modulated as follows:

$$\omega_b=\frac{\tilde{\omega}_b}{\sum_{b=1}^{B}\tilde{\omega}_b+\delta},\quad \tilde{\omega}_b=\omega_b^0\pi_b\left[0.70+0.30\frac{Q_b}{\text{median}(Q_b)+\delta}\right] \tag{7}$$

where ω_b^0 is the basic frequency-band weight, π_b is the frequency-band prior factor, and Q_b is the frequency-band quality factor estimated from the P- and S-window signal-to-noise ratio or effective-energy ratio. This design adjusts the contribution of each frequency band according to its observed signal quality instead of combining the bands with fixed weights.

To prevent different misfit terms from dominating the joint objective function because of dimensional and numerical scale differences, the inter-term effective weights are determined by the median scale of the candidate-solution set:

$$S_m=\text{median}_{\theta\in\Omega}\left[\Phi_m(\theta)\right]+\delta,\quad m=w,p,a,g \tag{8}$$

The original inter-term weights are then obtained from the basic scale factors and median-scale matching, and are further normalized as follows:

$$\lambda_m=\frac{\lambda_m^0/S_m}{\sum_{j\in\{w,p,a,g\}}\lambda_j^0/S_j},\quad m=w,p,a,g \tag{9}$$

where λ_m^0 is the basic scale factor used to specify the prior strength of each constraint term; the normalized λ_m satisfies $\sum_m \lambda_m=1$. This weighting mechanism combines the ideas of robust penalty and inter-term scale matching in inversion [20–23]. It simultaneously considers receiver-recording quality, frequency-band signal quality, and scale differences among objective-function terms, thereby limiting the undue influence of low-quality records, contaminated frequency bands, or any single misfit term on the full moment tensor solution.

2.3 Adaptive DC-Constrained Staged Moment Tensor Inversion

The full moment tensor model has high degrees of freedom and can easily amplify non-uniqueness under downhole observation conditions. If the degrees of freedom related to source type are not controlled, ISO and CLVD components may overfit noise or propagation-model errors [19, 24–26]. Therefore, the dominant shear mechanism constrained by the observations is first extracted in the pure-DC subspace. The pure-DC subspace is defined as:

$$\mathrm{D}_{DC}=\{\theta_{DC}=(s,d,r,\eta_{\mathbf{iso}}=0,\eta_{\mathbf{clvd}}=0,\gamma)\} \tag{10}$$

The top K candidate models with smaller objective-function values are then selected from this space to form the DC core set:

$$E_{DC}=\text{TopK}\{\Phi(\theta_{DC})\,|\,\theta_{DC}\in\mathrm{D}_{DC}\} \tag{11}$$

The DC core set is not an externally specified prior; rather, it comprises a group of low-degree-of-freedom reference solutions jointly constrained by three-component waveforms, first-motion polarity, and amplitude ratios. To illustrate how the skeleton constraint is calculated, let θ_j^{DC} denote the j-th core solution. The normalized guidance distance of a candidate solution θ relative to the DC skeleton is defined as:

$$D_G(\theta,E_{DC})=\min_j\left[\left(\frac{\Delta s_j}{\sigma_s}\right)^2+\left(\frac{\Delta d_j}{\sigma_d}\right)^2+\left(\frac{\Delta r_j}{\sigma_r}\right)^2+\left(\frac{\Delta z_j}{\sigma_z}\right)^2+\left(\frac{\Delta \gamma_j}{\sigma_\gamma}\right)^2\right]^{1/2} \tag{12}$$

where Δs_j, Δd_j, and Δr_j denote the minimum angular distances in strike, dip, and rake relative to the j-th DC elite solution, respectively; Δz_j and $\Delta\gamma_j$ denote the deviations in source depth and the velocity-scale correction parameter; and σ_s, σ_d, σ_r, σ_z, and σ_γ are normalization scales specified by the parameter search ranges or perturbation scales. If the event location is fixed, the depth term can be omitted.

On the basis of this distance, the adaptive DC-skeleton constraint term is written as:

$$J_g(\theta)=\mu_1 D_G^2(\theta,E_{DC})+\mu_2\kappa R_{ndc}(\theta)+\mu_3 C_{stab}(\theta) \tag{13}$$

where $R_{ndc}(\theta)$ represents the expression strength of the ISO/CLVD components and can be characterized by $\eta_{iso}^2+\eta_{clvd}^2$ or by its normalized form; $C_{stab}(\theta)$ represents the mechanism-stability penalty of the candidate solution under local perturbation; and κ is the explanatory capability of the DC skeleton for multiple types of observations. It can be determined by the integrated fitting level of the best-performing solution in the DC core set under waveform, polarity, and amplitude-ratio constraints:

$$\kappa=\text{clip}\left(1-\frac{1}{3}\sum_{m\in\{w,p,a\}}\frac{\Phi_m(\theta_{DC}^*)}{S_m},0,1\right) \tag{14}$$

A larger κ indicates that the low-degree-of-freedom DC skeleton already explains the observations well; in this case, a stronger restriction is imposed on non-DC component expression. A smaller κ indicates that a pure shear mechanism provides an insufficient explanation, and controlled contributions from the ISO/CLVD components are permitted.

3. METHOD VALIDATION

3.1 Synthetic Observation System and Test Data Construction

A downhole microseismic observation system is constructed with reference to the public Utah FORGE downhole monitoring scenario and related microseismic data [13], as shown in Figure 2. This observation system includes two vertical wells as monitoring wells and one horizontal well as the fracturing well. Under the observation-system and velocity-model conditions, four representative source-type microseismic events are set (see Figure 2(c)) to verify the effectiveness of the proposed method. Meanwhile, under noise interference and velocity perturbation, three fracturing stages with a total of 96 microseismic events are designed (see Figure 2(d)), and the moment tensor deviation angle and physically acceptable solution proportion are compared to evaluate the stability of the proposed method.

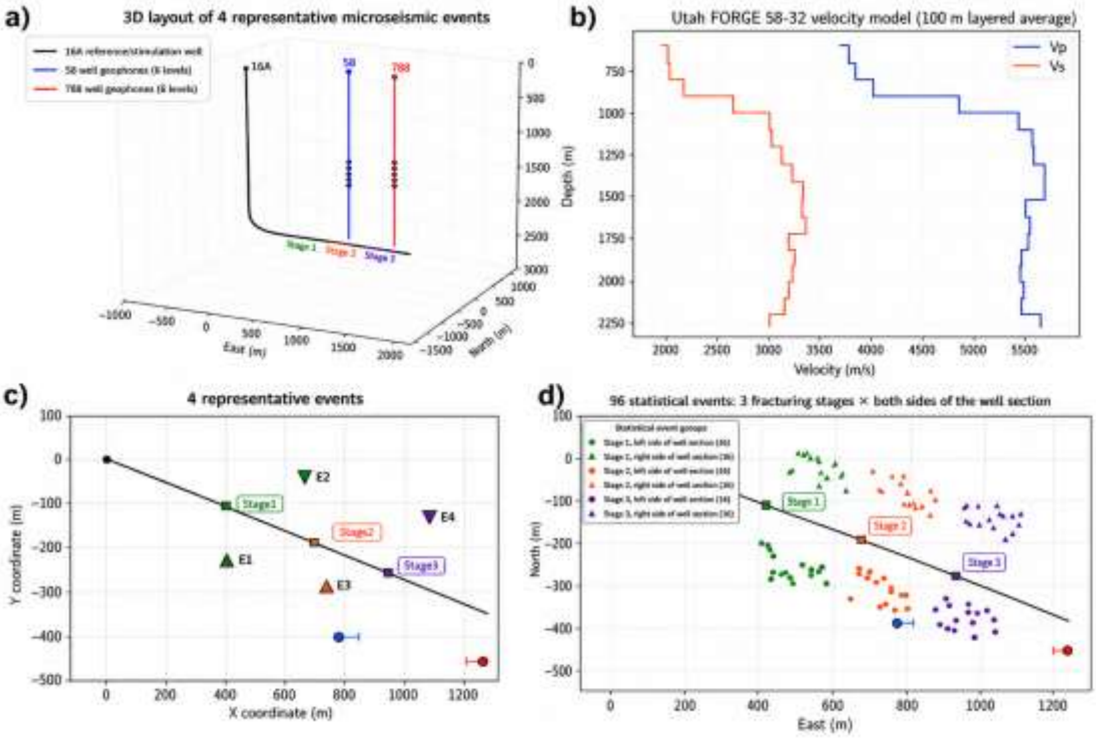

Figure 2. Downhole observation system, source locations, and velocity model: (a) three-dimensional spatial layout of the fracturing well, monitoring wells, and three fracturing stages; (b) Utah FORGE P-wave and S-wave velocity model; (c) planar distribution of representative source-type events; (d) planar distribution of 96 statistical events.

3.2 Parameter Settings and Comparison Methods

To ensure the repeatability of the numerical tests and clarify the distinction between fixed and adaptive parameters, the synthetic tests use three frequency bands of 20–40, 40–60, and 60–80 Hz, with basic frequency-band weights of (0.50, 0.30, 0.20) and a frequency-band prior factor of 1.0. The inter-term basic scale factors for the waveform, polarity, amplitude-ratio, and non-DC regularization terms are set to (1.00, 0.16, 0.035, 0.0020), respectively, and the DC core-set size is $\kappa = 6$. These values are fixed baseline settings for the synthetic tests; the frequency-band quality factors and inter-term effective weights are still adaptively calculated from the observation quality of each event and the candidate-solution set.

The waveform-matching method and the fixed-weight joint-constrained method are used as comparison methods. The waveform-matching method searches for the focal mechanism mainly according to waveform similarity in effective P- and S-wave windows [9–10]. The fixed-weight joint-constrained method further introduces P-wave first-motion polarity and S/P amplitude-ratio constraints on the basis of waveform matching [7–10], but it adopts fixed weights for different receiver records, frequency bands, and mechanism-sensitive features.

3.3 Effectiveness Test

Four microseismic sources (E1–E4) are set near the fracturing well, and their true source-mechanism parameters are specified (Table 1). E1 and E2 are used to examine the ability to control apparent non-DC components in DC-dominated events, whereas E3 and E4 are used to examine whether ISO/CLVD components in mixed-type events are excessively suppressed. Each event is first forward modeled using Eqs. (1) and (2) to generate three-component waveforms. P- and S-wave windows are extracted within the three frequency bands. The waveform, first-motion polarity, and S/P amplitude-ratio misfit terms are calculated using Eqs. (4)–(6), respectively. The frequency-band weights are updated using Eq. (7) according to the effective-signal quality of each band, and inter-term scale matching is completed using Eqs. (8)–(9). During inversion, the dominant shear mechanism is first searched in the pure-DC subspace shown in Eq. (10), and the top K DC candidate solutions are retained according to Eq. (11) to form the skeleton set. Eqs. (12)–(14) are then used to calculate the guidance distance and constraint strength of each candidate full moment tensor relative to the DC skeleton. Finally, the optimal moment tensor solution is determined by minimizing the joint objective function in Eq. (3). The waveform-fitting result for representative event E2 is shown in Figure 3.

Table 1. True source-mechanism parameters of the four representative source-type events.

Event ID	Type	Strike (°)	Dip (°)	Rake (°)	DC (%)	ISO (%)	CLVD (%)
E1	DC-dominated event	4.0	85.0	180.0	100.0	0.0	0.0
E2	DC-dominated event	99.3	80.0	-29.6	95.4	4.5	0.1
E3	Mixed-type event	264.6	63.1	49.8	48.3	24.8	26.9

Event ID	Type	Strike (°)	Dip (°)	Rake (°)	DC (%)	ISO (%)	CLVD (%)
E4	Mixed-type event	68.4	61.2	57.6	44.3	31.8	23.9

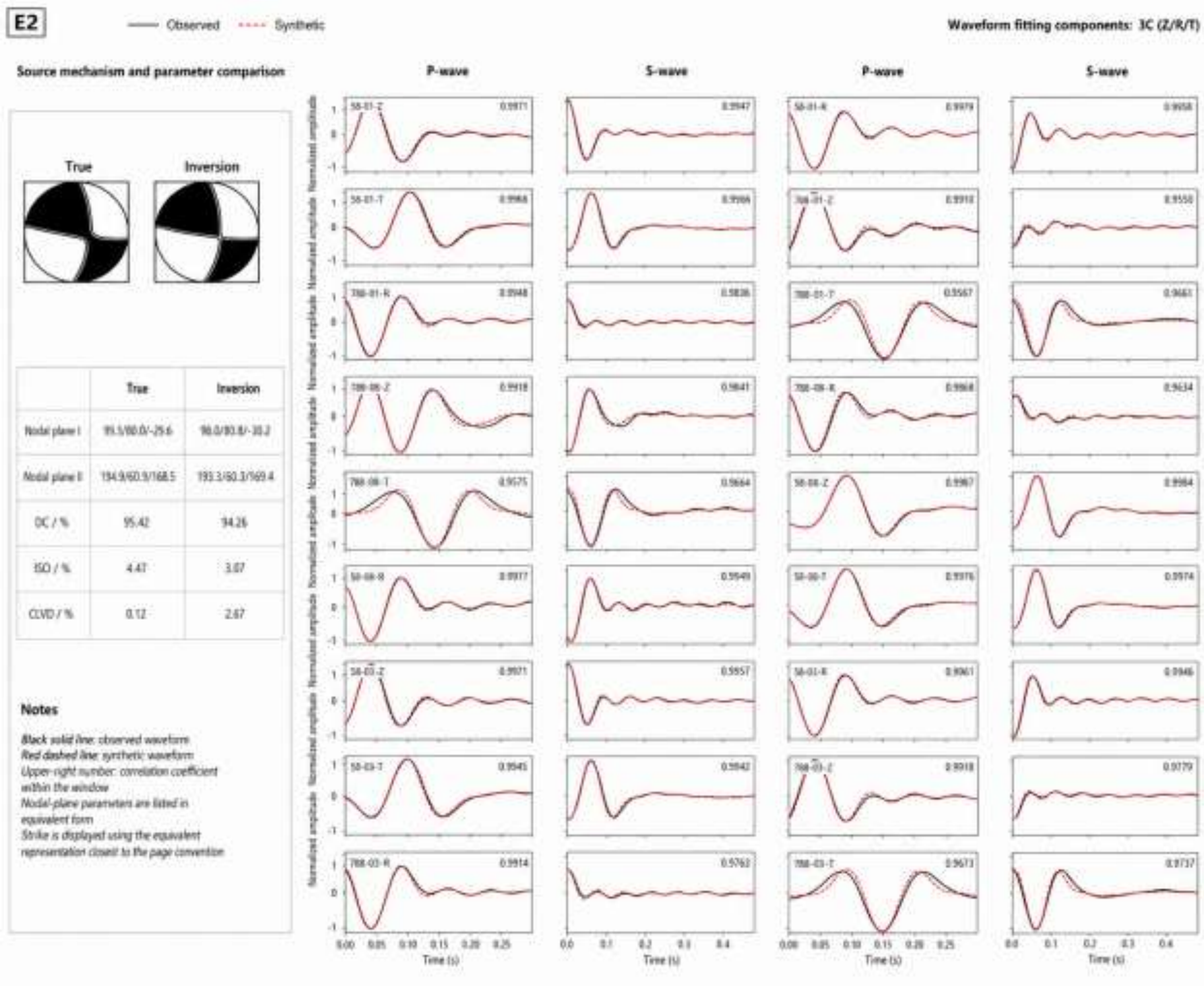

Figure 3. Representative three-component waveform-fitting result for event E2.

To further quantitatively compare the mechanism-recovery differences among the three methods for the representative source-type events, Table 2 lists the inversion results of the four events under the three methods.

Table 2. Comparison of inversion results of the three methods for four representative source-type events.

Event ID	Method	Strike (°)	Dip (°)	Rake (°)	DC (%)	ISO (%)	CLVD (%)	ω (°)
	Waveform matching	90.6	76.8	-139.5	69.48	28.16	2.35	44.46
E1	Fixed-weight	2.0	74.5	176.9	90.34	6.32	3.34	12.74
	QG-ADCC-MTI	2.3	75.2	177.7	96.39	0.29	3.32	10.94
	Waveform matching	85.8	88.6	-44.0	84.53	14.42	1.06	26.39
E2	Fixed-weight	102.8	86.0	-17.2	82.35	11.92	5.72	25.27
	QG-ADCC-MTI	98.0	80.8	-30.2	94.26	3.07	2.67	2.68
	Waveform matching	212.6	58.3	-64.6	77.26	12.86	9.88	44.94
E3	Fixed-weight	262.0	56.7	51.0	52.32	20.11	27.57	14.06
	QG-ADCC-MTI	264.3	62.3	49.3	47.94	27.45	24.61	3.29
	Waveform matching	67.0	63.6	19.9	70.10	9.80	20.10	51.43
E4	Fixed-weight	81.3	46.6	25.4	57.30	22.55	20.15	18.93
	QG-ADCC-MTI	70.4	62.1	56.7	48.06	27.65	24.29	7.29

Note: Strike, dip, and rake are all expressed using nodal plane I. **ω** is the deviation angle between the inverted and true moment tensors. The method names correspond to the waveform-matching method, the fixed-weight joint-constrained method, and the QG-ADCC-MTI method.

For DC-dominated events, the proposed method more effectively suppresses apparent non-double-couple components caused by noise and local waveform errors. For E1, the waveform-matching method and the fixed-weight joint-constrained method obtain DC components of 69.48% and 90.34%, respectively, whereas the proposed method increases the DC component to 96.39%, controls the ISO component at 0.29%, and obtains a moment tensor deviation angle of 10.94°. For E2, the deviation angle of the proposed method is only 2.68°, which is markedly lower than those of the waveform-matching method (26.39°) and the fixed-weight joint-constrained method (25.27°). Its DC/ISO/CLVD proportions are 94.26%/3.07%/2.67%, in close agreement with the prescribed DC-dominated source type.

For mixed-type events, the proposed method does not indiscriminately force mixed-type events toward high-DC solutions; instead, it preserves the DC/ISO/CLVD source-type proportions. For E3, the waveform-matching method clearly overestimates the DC component to 77.26%. Although the fixed-weight joint-constrained method improves the result, its deviation angle is still 14.06°. The proposed method obtains DC/ISO/CLVD proportions of 47.94%/27.45%/24.61% with a deviation angle of 3.29°, which is closest to the true proportions. For E4, the proposed method obtains DC/ISO/CLVD proportions of 48.06%/27.65%/24.29% and a deviation angle of 7.29°, also outperforming the two comparison methods. These results indicate that QG-ADCC-MTI can suppress apparent non-DC leakage in DC-dominated events while retaining reasonable ISO/CLVD components in mixed-type events.

3.4 Stability Test

In Figure 2(d), three fracturing stages are set, and each stage contains 32 events. The horizontal position, depth, strike, dip, rake, and ISO/CLVD components of each event are randomly perturbed within the preset ranges corresponding to each source type, thereby forming a synthetic event set that spans variations in both source type and spatial coverage.

The stability tests include two groups: noise interference and velocity perturbation. In the noise-interference test, independent zero-mean Gaussian noise is added to each receiver trace, with the noise standard deviation set to 10%, 25%, or 40% of the standard deviation of the corresponding clean synthetic trace. This scaling is applied under the same velocity model to examine stability when first-motion polarity, local waveform morphology, and S/P amplitude ratios are affected by noise. In the velocity-perturbation test, ±3%, ±8%, and ±15% layered velocity perturbations are introduced into the inversion velocity model to examine the influence of P- and S-window phase shifts, amplitude responses, and frequency-band energy variations on the inversion results. Each perturbation condition is repeated three times, and every perturbed sample is processed using the same inversion workflow as in the effectiveness tests.

The moment tensor deviation angle, moment tensor similarity, waveform correlation coefficient, and physically acceptable solution proportion are used to evaluate inversion stability. The moment tensor deviation angle, ω, measures the overall angular difference between the inverted and true moment tensors and is expressed as:

$$\omega = \cos^{-1}\left(\frac{\langle M_{\mathbf{inv}}, M_{\mathbf{true}}\rangle}{\|M_{\mathbf{inv}}\|\|M_{\mathbf{true}}\|}\right)\frac{180}{\pi} \tag{15}$$

where $M_{\mathbf{true}}$ and $M_{\mathbf{inv}}$ denote the true and inverted moment tensors, respectively; $\langle \cdot,\cdot \rangle$ denotes their Frobenius inner product; and $\|\cdot\|$ denotes the Frobenius norm. A smaller moment tensor deviation angle indicates a mechanism closer to the true mechanism. Angular differences between focal mechanisms are also widely used to assess mechanism consistency [27]. To support the criterion for physically acceptable solutions, the moment tensor similarity is further defined as:

$$sim = \frac{1}{2}\left[1 + \frac{\langle M_{\mathbf{inv}}, M_{\mathbf{true}}\rangle}{\|M_{\mathbf{inv}}\|\|M_{\mathbf{true}}\|}\right] \tag{16}$$

where sim ranges from 0 to 1, with values closer to 1 indicating that the inverted moment tensor is more similar to the true moment tensor. To quantify the agreement between synthetic and observed waveforms, this paper further introduces the waveform correlation coefficient CC, calculated from the normalized cross-correlation between observed and synthetic waveforms within effective P- and S-wave windows. Values closer to 1 indicate higher waveform-fitting consistency. To prevent failed samples from being obscured by mean-value statistics, a binary criterion is adopted to evaluate the inversion results. Solutions satisfying $\omega \le 35\%$, $sim \ge 0.80$, $CC \ge 0.75$ are classified as physically acceptable solutions, whereas all other solutions are classified as unacceptable. The similarity and waveform-correlation thresholds are empirical screening limits applied consistently to all three methods.

For the descriptive comparison in Figure 4, this study treats deviation angles below 30°, from 30° to 45°, and above 45° as low-, intermediate-, and high-deviation ranges, respectively. These empirical ranges are used only for qualitative interpretation. The physically acceptable-solution statistics in Figure 5 are defined independently by the joint criterion of ω ⩽ 35°, sim ⩾ 0.80, and CC ⩾ 0.75.

Under noise interference, the median deviation angle is approximately 65°–70° for the waveform-matching method and 30°–40° for the fixed-weight joint-constrained method, whereas it remains at 18°–22° for the proposed method, whose distribution is also more concentrated. Under velocity perturbation, the median angle remains approximately 68°–72° for the waveform-matching method, increases to approximately 50° for the fixed-weight joint-constrained method at ±15% perturbation, and remains at approximately 18°–25° for the proposed method across all perturbation levels. These results indicate that the proposed method reduces mechanism deviation and improves the stability of full moment tensor inversion under both noise and velocity-model errors.

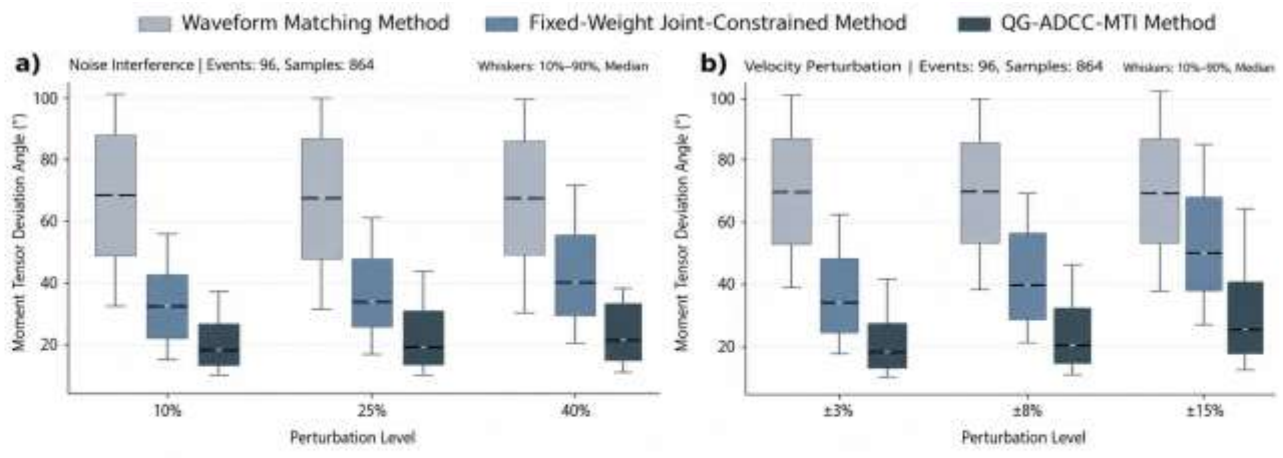

Figure 4. Variations in moment tensor deviation angle under different conditions: (a) noise interference; (b) velocity perturbation.

Figure 5 shows the proportions of physically acceptable mechanism solutions obtained by the three methods under different perturbation conditions. Under noise interference, the waveform-matching and fixed-weight joint-constrained methods yield proportions ranging from 0.12 to 0.14 and from 0.39 to 0.57, respectively, whereas QG-ADCC-MTI maintains proportions ranging from 0.77 to 0.86. Under velocity perturbation, the corresponding proportions range from 0.08 to 0.09, from 0.21 to 0.51, and from 0.66 to 0.86, respectively.

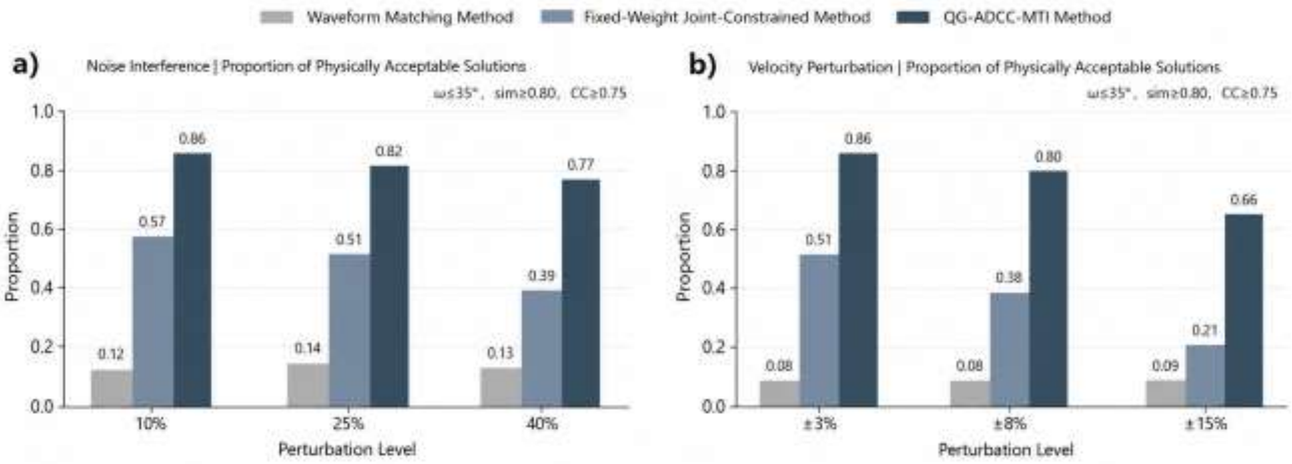

Figure 5. Proportions of physically acceptable mechanism solutions under different perturbation conditions: (a) noise interference; (b) velocity perturbation.

4. CONCLUSIONS

To address the susceptibility of downhole full moment tensor inversion to receiver-recording quality variations, velocity-model errors, and local waveform residuals, this paper proposes a quality-guided and adaptive DC-constrained microseismic moment tensor inversion method. The method combines receiver-recording quality weights and frequency-band quality modulation with an adaptive DC skeleton constraint. It regulates ISO/CLVD contributions according to the observational support for a stable dominant shear mechanism, thereby reducing the risk that noise and modeling errors are misinterpreted as non-double-couple components. The effectiveness tests show that the proposed method suppresses spurious ISO/CLVD contributions in pure-DC and DC-dominated events while preserving reasonable source-type proportions in mixed-type events containing genuine ISO/CLVD contributions. Thus, the method does not indiscriminately force all events toward high-DC solutions but adapts the source-type constraints to the observational support for non-double-couple components. In the stability tests, under 10%, 25%, and 40% noise levels, the physically acceptable solution proportions of the proposed method are 0.86, 0.82, and 0.77, respectively, which are significantly higher than those of the fixed-weight joint-constrained method (0.57, 0.51, and 0.39) and the waveform-matching method (0.12, 0.14, and 0.13). Under ±3%, ±8%, and ±15% velocity-model perturbations, the corresponding proportions are 0.86, 0.80, and 0.66, respectively, again outperforming both comparison methods.

5. REFERENCES

[1] C. T. Montgomery and M. B. Smith, "Hydraulic fracturing: History of an enduring technology," Journal of Petroleum Technology, vol. 62, no. 12, pp. 26–40, 2010, doi: 10.2118/1210-0026-JPT.

[2] S. C. Maxwell, Microseismic Imaging of Hydraulic Fracturing: Improved Engineering of Unconventional Shale Reservoirs. Tulsa, OK, USA: Society of Exploration Geophysicists, 2014, doi: 10.1190/1.9781560803164.

[3] D. W. Eaton, Passive Seismic Monitoring of Induced Seismicity: Fundamental Principles and Application to Energy Technologies. Cambridge, UK: Cambridge University Press, 2018, doi: 10.1017/9781316535547.

[4] N. R. Warpinski, "Understanding hydraulic fracture growth, effectiveness, and safety through microseismic monitoring," in Effective and Sustainable Hydraulic Fracturing, A. P. Bunger, J. McLennan, and R. Jeffrey, Eds. Rijeka, Croatia: IntechOpen, 2013, doi: 10.5772/55974.

[5] F. Song and M. N. Toksoz, "Full-waveform based complete moment tensor inversion and source parameter estimation from downhole microseismic data for hydrofracture monitoring," Geophysics, vol. 76, no. 6, pp. WC103–WC116, 2011, doi: 10.1190/GEO2011-0027.1.

[6] H. Li, X. Chang, J. Hao, and Y. Wang, "Comparison of single-well microseismic focal mechanism inversions with different source models," Bulletin of the Seismological Society of America, vol. 111, no. 6, pp. 3103–3117, 2021, doi: 10.1785/0120210070.

[7] J. L. Hardebeck and P. M. Shearer, "A new method for determining first-motion focal mechanisms," Bulletin of the Seismological Society of America, vol. 92, no. 6, pp. 2264–2276, 2002, doi: 10.1785/0120010200.

[8] J. L. Hardebeck and P. M. Shearer, "Using S/P amplitude ratios to constrain the focal mechanisms of small earthquakes," Bulletin of the Seismological Society of America, vol. 93, no. 6, pp. 2434–2444, 2003, doi: 10.1785/0120020236.

[9] J. Li, H. Zhang, H. S. Kuleli, and M. N. Toksoz, "Focal mechanism determination using high-frequency waveform matching and its application to small magnitude induced earthquakes," Geophysical Journal International, vol. 184, no. 3, pp. 1261–1274, 2011, doi: 10.1111/j.1365-246X.2010.04903.x.

[10] Y. Tan, J. Hu, H. Zhang, et al., "Focal mechanism determination of hydraulic-fracturing-induced earthquakes using full-waveform matching," Chinese Journal of Geophysics, vol. 62, no. 11, pp. 4417–4436, 2019, doi: 10.6038/cjg2019M0516. (in Chinese)

[11] J. Lecoulant, Y. Ma, J. Dettmer, and D. Eaton, "Strain-based forward modeling and inversion of seismic moment tensors using distributed acoustic sensing (DAS) observations," Frontiers in Earth Science, vol. 11, article 1176921, 2023, doi: 10.3389/feart.2023.1176921.

[12] H. Li, X. Chang, and J. Hao, "Hydraulic fracturing shear/tensile/compressive crack investigation using microseismic data," Remote Sensing, vol. 16, no. 11, article 1902, 2024, doi: 10.3390/rs16111902.

[13] I. Vera Rodriguez, T. Coleman, D. Podrasky, C. Maldaner, Y. Ma, J. Ajo-Franklin, and the FOGMORE@FORGE Team, "DAS moment tensor inversion analysis for microseismic events observed during the 2023 circulation tests at Utah FORGE," in Proceedings of the 50th Workshop on Geothermal Reservoir Engineering, Stanford University, Stanford, CA, USA, Feb. 10–12, 2025, SGP-TR-229.

[14] M. L. Jost and R. B. Herrmann, "A student's guide to and review of moment tensors," Seismological Research Letters, vol. 60, no. 2, pp. 37–57, 1989, doi: 10.1785/gssrl.60.2.37.

[15] B. R. Julian, A. D. Miller, and G. R. Foulger, "Non-double-couple earthquakes 1. Theory," Reviews of Geophysics, vol. 36, no. 4, pp. 525–549, 1998, doi: 10.1029/98RG00716.

[16] V. Vavrycuk, "Moment tensor decompositions revisited," Journal of Seismology, vol. 19, no. 1, pp. 231–252, 2015, doi: 10.1007/s10950-014-9463-y.

[17] K. Aki and P. G. Richards, Quantitative Seismology, 2nd ed. Sausalito, CA, USA: University Science Books, 2002.

[18] L. S. Zhao and D. V. Helmberger, "Source estimation from broadband regional seismograms," Bulletin of the Seismological Society of America, vol. 84, no. 1, pp. 91–104, 1994.

[19] S. E. Minson and D. S. Dreger, "Stable inversions for complete moment tensors," Geophysical Journal International, vol. 174, no. 2, pp. 585–592, 2008, doi: 10.1111/j.1365-246X.2008.03797.x.

[20] P. J. Huber, "Robust estimation of a location parameter," The Annals of Mathematical Statistics, vol. 35, no. 1, pp. 73–101, 1964, doi: 10.1214/aoms/1177703732.

[21] A. Tarantola, Inverse Problem Theory and Methods for Model Parameter Estimation. Philadelphia, PA, USA: Society for Industrial and Applied Mathematics, 2005, doi: 10.1137/1.9780898717921.

[22] W. Menke, Geophysical Data Analysis: Discrete Inverse Theory, 3rd ed. Waltham, MA, USA: Academic Press, 2012.

[23] A. Fichtner, Full Seismic Waveform Modelling and Inversion. Berlin, Germany: Springer, 2011, doi: 10.1007/978-3-642-15807-0.

[24] J. D. Pesicek, K. Cieslik, M. A. Lambert, P. Carrillo, and B. Birkelo, "Dense surface seismic data confirm non-double-couple source mechanisms induced by hydraulic fracturing," Geophysics, vol. 81, no. 6, pp. KS207–KS217, 2016, doi: 10.1190/geo2016-0192.1.

[25] J. Tang, L. Wen, C. Li, and R. Qi, "Hydraulic-fracturing shear-tensile microseismic focal mechanism moment tensor inversion," Oil Geophysical Prospecting, vol. 54, no. 4, pp. 826–835, 2019, doi: 10.13810/j.cnki.issn.1000-7210.2019.04.013. (in Chinese)

[26] L. Liu, W. Song, X. Yang, J. Hu, L. Dong, and Z. Yu, "Single-well microseismic focal mechanism inversion under shear-tensile source constraint," Oil Geophysical Prospecting, vol. 56, no. 5, pp. 1093–1104, 2021, doi: 10.13810/j.cnki.issn.1000-7210.2021.05.016. (in Chinese)

[27] Y. Cheng, R. M. Allen, and T. Taira, "A new focal mechanism calculation algorithm (REFOC) using inter-event relative radiation patterns: Application to the earthquakes in the Parkfield area," Journal of Geophysical Research: Solid Earth, vol. 128, no. 3, article e2022JB025006, 2023, doi: 10.1029/2022JB025006.